

Simple yet clear local evidence for the tetrahedral triple- Q magnetic ground state in the triangular antiferromagnet $\text{Co}_{1/3}\text{NbS}_2$

Yiwen Dong ¹, Bo Zhang,¹ Yantao Cao ^{1,2}, Hanjie Guo,² Wei Ren,¹ Anmin Zhang,¹ ZhenHua Li,³ Zhengqing Wei,⁴ Haoliang Liu,⁴ Liyun Tang,¹ Hua Pang,¹ Fashen Li,¹ and Zhiwei Li ^{1,*}

¹Key Lab for Magnetism and Magnetic Materials of the Ministry of Education, School of Physical Science and Technology, Lanzhou University, Lanzhou 730000, Gansu, China

²Songshan Lake Materials Laboratory, Dongguan 523808, Guangdong, China

³Lanzhou Center for Theoretical Physics, Key Laboratory of Quantum Theory and Applications of MOE, Key Laboratory of Theoretical Physics of Gansu Province, Lanzhou University, Lanzhou 730000, Gansu, China

⁴Guangdong Provincial Key Laboratory of Semiconductor, Optoelectronic Materials and Intelligent Photonic Systems, School of Science, Harbin Institute of Technology (Shenzhen), Shenzhen 518055, China



(Received 18 October 2023; revised 1 January 2024; accepted 7 February 2024; published 1 March 2024)

In this work, we demonstrate a simple yet effective procedure for identifying the exotic tetrahedral triple- Q magnetic ordering over the domain averaged collinear single- Q magnetic state for the triangular antiferromagnet $\text{Co}_{1/3}\text{NbS}_2$. Our density functional theory (DFT) calculations show that the hyperfine magnetic field exhibits a significant anisotropic dependence on the angle between the spin direction and the c -axis, which means that the atoms with different spin directions in the triple- Q state can be divided into two subgroups with a ratio of 1:3 that can be distinguished by local probing methods. Mössbauer spectroscopy measurements on $(\text{Co}_{0.99}^{57}\text{Fe}_{0.01})_{1/3}\text{NbS}_2$ crystals confirm exactly our DFT predictions and thus give possible evidence of the tetrahedral triple- Q magnetic state. These results provide important insights into the magnetic ground state of $\text{Co}_{1/3}\text{NbS}_2$, which shall shed light on the understanding of the anomalous Hall effect in $\text{Co}_{1/3}\text{NbS}_2$ and other related materials.

DOI: [10.1103/PhysRevB.109.094401](https://doi.org/10.1103/PhysRevB.109.094401)

I. INTRODUCTION

Exotic non-collinear magnetism, including spiral/helical magnetism [1–3], chiral antiferromagnetism [4–6], and magnetic skyrmions [7,8], usually lead to novel properties and functionalities and thus hold great promise for next generation spintronic applications [8,9]. For instance, the transition-metal intercalated dichalcogenide system $M_x(\text{Nb,Ta})\text{S}_2$ (M is 3d transition metal) with a metallic triangular lattice have been attracting much attention due to their various non-collinear magnetic structures and resulting exotic properties, such as the anomalous Hall effect (AHE) [5,6], electrical magneto-chiral effect [10], and magnetic soliton confinement [11]. In contrast to the normal collinear magnetic states, the microscopic mechanism of these states is less clear. It is generally believed that they are induced by magnetic frustration arising from competing interactions and/or lattice geometry. Moreover, the specific non-collinear magnetic structures of these compounds also depend highly on the intercalated M element and the exact intercalation level x [1,2,12]. For example, chiral helimagnetism was observed for $\text{Cr}_{1/3}\text{NbS}_2$ [1–3] and $\text{Mn}_{1/3}\text{NbS}_2$ [12]. A-type antiferromagnetic (AFM) ordering with a subtle canting of the XY spins in the c -axis was observed for $\text{V}_{1/3}(\text{Nb, Ta})\text{S}_2$ [13]. For Fe_xNbS_2 [14], distinct AFM stripe and zigzag orders with wave vectors of (0.5, 0, 0) and (0.25,

0.5, 0), respectively, indexed in the lattice shown in Fig. 1(a) were found depending on the value of x . Recently, it was also reported that $\text{Ni}_{1/3}\text{NbS}_2$ develops an AFM helical order with a very long period of $33c$ along the c -axis whereas the sister compound $\text{Ni}_{1/3}\text{TaS}_2$ orders in the simple A-type magnetic structure [15].

More interestingly, the $\text{Co}_{1/3}\text{NbS}_2$ might be the most promising candidates to exhibit quantized AHE since an extremely large AHE with a Hall conductivity comparable to e^2/h per single layer was discovered in this system [5,6]. However, understanding of the observed AHE, which requires the knowledge of the magnetic structure, is still challenging [16–18]. Early neutron scattering measurement has reported collinear AFM structure with a complicated domain structure for $\text{Co}_{1/3}\text{NbS}_2$ and a possible 120° ordering [see Fig. 1(c)] with wave vector (1/3, 1/3, 0) for $\text{Co}_{1/3}\text{TaS}_2$ [19]. Recent neutron scattering experiments, however, have shown that more complex magnetic orderings could also be possible [16,17]. These experiments have revealed magnetic peak positions at the M -points of the Brillouin zone ((0.5, 0, 0) and symmetry related positions) for both $\text{Co}_{1/3}\text{NbS}_2$ [16] and $\text{Co}_{1/3}\text{TaS}_2$ [17] in contrast to the early result at (1/3, 1/3, 0) [19], suggesting that $\text{Co}_{1/3}\text{TaS}_2$ does not exhibit the so-called 120° magnetic ordering.

These results can be interpreted as either a single- Q [see Fig. 1(b)] magnetic ordering with three equally weighted magnetic domains that differ by a $\pm 120^\circ$ rotation about the z -axis (C_{3z}) axis (C_{3z}) or a single-domain triple- Q magnetic

*zweili@lzu.edu.cn

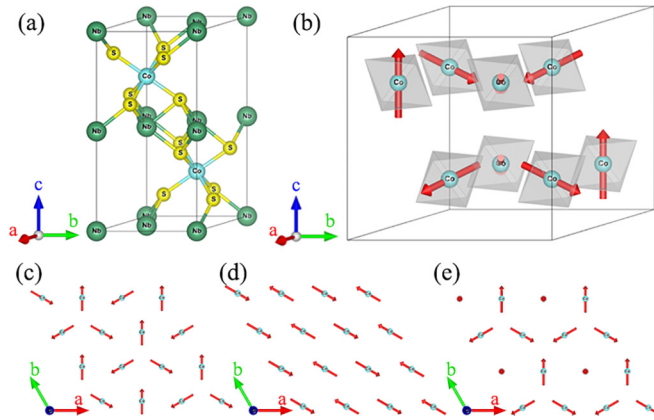


FIG. 1. (a) Crystal structure of $\text{Co}_{1/3}\text{NbS}_2$. (b) Magnetic unit cell ($2 \times 2 \times 1$ of the structural unit cell) of the tetrahedral triple-Q ($\chi_{ijk} > 0$ [17]) magnetic structure showing only the Co atoms with their spins for clear view. (c) Schematics of the coplanar 120° 3-sublattice magnetic ordering, (d) the single-Q 2-sublattice stripe magnetic ordering, and (e) the 4-sublattice tetrahedral triple-Q magnetic ordering (same with (b)) showing only one Co triangular layer. Note that the spins shown in (c) and (d) could be purely in plane or c -axis canted. This figure was drawn by using the VESTA [20] software.

ordering [see Figs. 1(b) and 1(e)]. The tetrahedral triple-Q magnetic ordering, as shown in Fig. 1(b) that represents the short-wavelength limit of a magnetic skyrmion structure, is predicted to appear in the metallic triangular lattice when effective four-spin interactions arising from the exchange interaction between itinerant electrons and localized spins were considered [21–23]. It was first observed in the *hcp*-Mn monolayer samples [24] by spin-polarized scanning tunneling microscopy, and recently in bulk samples of $\text{Co}_{1/3}\text{NbS}_2$ and $\text{Co}_{1/3}\text{TaS}_2$ [17,25] by neutron scattering measurements. Distinguishing between the domain averaged single-Q and triple-Q magnetic state in bulk form by experiments, however, is challenging. It requires detailed measurements of higher order neutron scattering peaks, comprehensive analysis of the scattering peaks in different neutron spin polarization channels, or analysis of the magnon symmetries along certain trajectories in the magnetic Brillouin zone [17,25,26], all of which need to coalign significant amounts of crystals due to the weak signal of these kinds of measurements.

In this work, we demonstrate a simple local probe procedure to identify such a triple-Q state with respect to the domain averaged single-Q state in the $\text{Co}_{1/3}\text{NbS}_2$ compound. As an important complement to the neutron scattering method, we exploit the fact that these two states might exhibit different local properties due to different local spin orientations. Our theoretical calculations predict a significant anisotropic hyperfine magnetic field for the different spin-oriented atoms in the triple-Q state that can be measured by local probing methods. Our Mössbauer spectroscopy measurements on $(\text{Co}_{0.99}\text{Fe}_{0.01})_{1/3}\text{NbS}_2$ crystals at 4.2 K confirm exactly our predictions and thus support the triple-Q magnetic ordering over the domain averaged single-Q magnetic ordering in this compound.

II. DFT CALCULATIONS

Let us first consider the two magnetic ground states as shown in Figs. 1(d) and 1(e), which produce the same neutron diffraction pattern, by density functional theory (DFT). The crystal structure was first optimized by using the Vienna *ab initio* simulation package (VASP) code [28,29]. All other calculations were done using the optimized crystal structure with the ELK code [30], which is an all electron code implemented using the full-potential linearized augmented plane wave method. Details of the parameters used in our DFT calculation, sample preparation, and characterization details are given in the Supplemental Material [27] (see also references therein [31–38]). Consistent with earlier work [16], the total energy for the single-Q and coplanar 120° magnetic states are found to be 7.91 meV and 18.36 meV, respectively, higher than that of the triple-Q state. Spin orbital coupling (SOC) effects were found to be small in earlier studies [16,18,39] since the bands of interest are dominated by Co $3d$ orbitals with weak SOC. However, an orbital moment of $\sim 0.1 \mu_B$ was calculated to be parallel to the Co spins in our case if SOC were considered. The effect of such an orbital moment should produce a reduction of the hyperfine fields [40] for all the atoms in the calculated cell leading to minor contributions to the anisotropy of the calculated hyperfine field (see Fig. S3 in the Supplemental Material [27]).

Next, we calculated the local hyperfine parameters at the Co site, such as the isomer shift (δ), electric field gradient (EFG) [principal component V_{zz} and asymmetry parameter $\eta = (V_{yy} - V_{xx})/V_{zz}$], and hyperfine magnetic field (B_{hf}), which can be probed using hyperfine interactions by Mössbauer spectroscopy and/or other microscopic methods [41] such as nuclear magnetic resonance (NMR), perturbed angular correlation (PAC), etc.. For the collinear single-Q state (whether spins canted to the c axis or not), our calculations show that all the Co atoms are equivalent, thus exhibiting the same calculated values of the local hyperfine parameters for all eight atoms in our $2 \times 2 \times 1$ cell. This means that only one subspectrum is enough to model the Mössbauer data in experiments. On the other hand, for the noncollinear triple-Q state, the eight atoms are divided into four sublattices from a symmetry point of view. However, from our calculations, the local hyperfine parameters can be divided into two subgroups with one subgroup (SP1) for the two atoms with their spins directed along the c axis and another subgroup (SP2) for the remaining six atoms, see Figs. 1(b) and 1(e). The main difference for the two subgroups is the calculated hyperfine magnetic field with $B_{\text{hf}} \sim 10$ T for SP1 and $B_{\text{hf}} \sim 16$ T for SP2. Other hyperfine parameters, δ and V_{zz} , exhibit similar values for all eight atoms (see Table. S2 in the Supplemental Material [27]). These results suggest that the hyperfine coupling tensor \mathbf{A} might be highly anisotropic (note that $\mathbf{B}_{\text{hf}} \propto \mathbf{A} \cdot \boldsymbol{\mu}_{\text{eff}}$). Therefore, one should observe two different hyperfine magnetic fields with a probability ratio of 1:3 in the Mössbauer experiments for the triple-Q state.

The above super-cell calculations suggest that the local hyperfine parameters might depend on the direction of the Co spins. To clear this out, we made further calculations by fixing the spins along various directions using the $1 \times 1 \times 1$ single

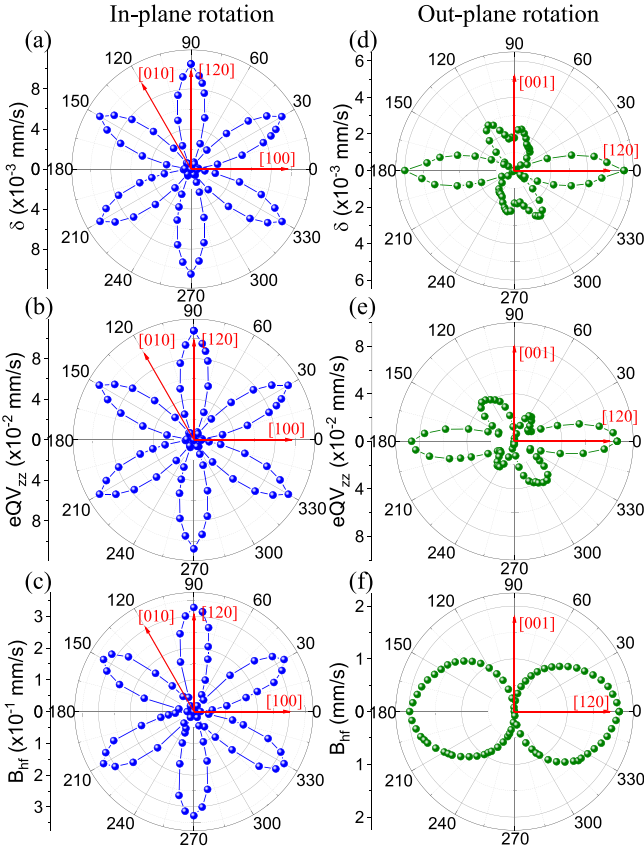


FIG. 2. Calculated (a)–(c) in-plane and (d), (e) out-of-plane anisotropic dependence of the isomer shift, δ , electric quadrupole coupling constant, eQV_{zz} , and the hyperfine magnetic field, B_{hf} , on the Co atom spin directions. These data were obtained by subtracting the smallest value in the corresponding rotation plane. Data in (a) and (d) were obtained by using the calculated contact charge density at the Co nucleus with a conversion factor of $0.4 \text{ mm s}^{-1} \text{ a.u.}^3$ (see details in the Supplemental Material [27]). The B_{hf} data in (c) and (f) were multiplied by a factor of $0.323 \text{ mm s}^{-1} \text{ T}^{-1}$ to clearly show how the anisotropy of B_{hf} will manifest itself in real Mössbauer experiments. These calculations were done with $1 \times 1 \times 1$ structural unit cell other than the $2 \times 2 \times 1$ super-cell to save computational time. Arrows in the figure indicate the crystallographic directions.

unit cell. Collinear and antiparallel alignment between the two spins in the cell were set in these calculations and the resulting hyperfine parameters are close to the corresponding ones in our $2 \times 2 \times 1$ super-cell calculations. The calculated in-plane and out-of-plane anisotropies of the δ , electric quadrupole coupling constant, eQV_{zz} , and B_{hf} are summarized in Fig. 2. It is clear that both the in-plane and out-of-plane anisotropies of the δ and eQV_{zz} are rather small (contribution to the peak shifts in real Mössbauer experiments are all below the value of $\sim 0.1 \text{ mm/s}$, which is much smaller than the natural line width of the ^{57}Fe isotope $\sim 0.19 \text{ mm/s}$ [42]). For the in-plane anisotropy of the B_{hf} shown in Fig. 2(c), the resulting peak shift is comparable to the the natural line width, which might lead to a broadening of the observed Mössbauer spectra. On the other hand, the out-of-plane anisotropy of the B_{hf} is significant, which would shift the Mössbauer absorption peaks by about $\sim 2 \text{ mm/s}$ if the spins were changing from within the

ab plane to the c -axis direction, see Fig. 2(f). These results explain well our super-cell calculations where the four sublattices in the triple-Q state are divided into two subgroups. Importantly, these calculations indicate that the triple-Q state can be well resolved from the multidomain averaged single-Q state by Mössbauer spectroscopy or other local probing methods due to the out-of-plane anisotropic dependence of the local hyperfine field B_{hf} on the spin directions of the Co atoms.

III. MÖSSBAUER SPECTROSCOPY MEASUREMENTS

In order to be able to make Mössbauer spectroscopy measurements, the ^{57}Fe probing nuclei need to be doped into the Co site of the $\text{Co}_{1/3}\text{NbS}_2$ crystal. Therefore, $\text{Co}_{1/3}\text{NbS}_2$ and $(\text{Co}_{0.99}\text{Fe}_{0.01})_{1/3}\text{NbS}_2$ single crystals were grown using the chemical vapor transport method similar to other reports [5,6]. The quality of our crystals were checked by structural, magnetic, and transport measurements as shown in Figs. S4–S7. Importantly, the $(\text{Co}_{0.99}\text{Fe}_{0.01})_{1/3}\text{NbS}_2$ crystals exhibit similar AHE to that of the pristine $\text{Co}_{1/3}\text{NbS}_2$ crystals [5,6] with an AFM transition temperature of $T_N \sim 28 \text{ K}$. The $(\text{Co}_{0.99}\text{Fe}_{0.01})_{1/3}\text{NbS}_2$ crystals were then cleaved into thin pieces with thicknesses in the range of $30\sim 40 \mu\text{m}$ for our Mössbauer spectroscopy measurements. Mössbauer spectra were taken in the temperature range of $4.2\sim 300 \text{ K}$ with a closed-cycle cryostat. The room temperature data, as shown in Fig. 3(a), exhibits an asymmetric doublet spectrum which can be well fitted with only one subspectrum in agreement with the only $^{57}\text{Fe}/\text{Co}$ crystallographic site in the crystal structure. The determined spectral line width is rather narrow, $\sim 0.258(5) \text{ mm/s}$, indicating good crystal quality consistent with other characterizations. From our DFT calculations and symmetry analysis, the asymmetry parameter η of the EFG is zero and V_{zz} is along the c axis. This is consistent with the fitted intensity ratio of the high temperature spectra shown in Fig. 3(a) and Fig. S8, which is close to the theoretical value of three for the V_{zz} directed along the c axis.

The Mössbauer spectrum taken at 4.2 K is shown in Figs. 3(b) and 3(c) together with different fitting models. As shown in Fig. 3(b), we first tried to fit the data with only one subspectrum corresponding to the collinear single-Q state shown schematically in Fig. 1(d). Clearly, the matching between the theoretical curve and the experimental data is bad [see the second, third, and fourth peaks from left to right in Fig. 3(b)]. This result is clearly inconsistent with the collinear single-Q magnetic structure. With a careful check of the experimental data, one finds an inhomogeneous line broadening of the sextet with the most inner peaks (third and fourth peaks) much narrower than the outer peaks (first and second). The inhomogeneous line broadening effect is usually found for samples with hyperfine magnetic field distributions [42–45]. Although the intercalated Co atoms are known to form the so-called $\sqrt{3} \times \sqrt{3}$ ordered phase [17,19], disorder to some extent can not be avoided. This is especially true when the intercalation level deviate from the exact value of $1/3$ [14,46]. Early Mössbauer studies on Fe_xNbS_2 have also reported distribution of the hyperfine magnetic field [47]. Therefore, we tried to model the experimental data using hyperfine field

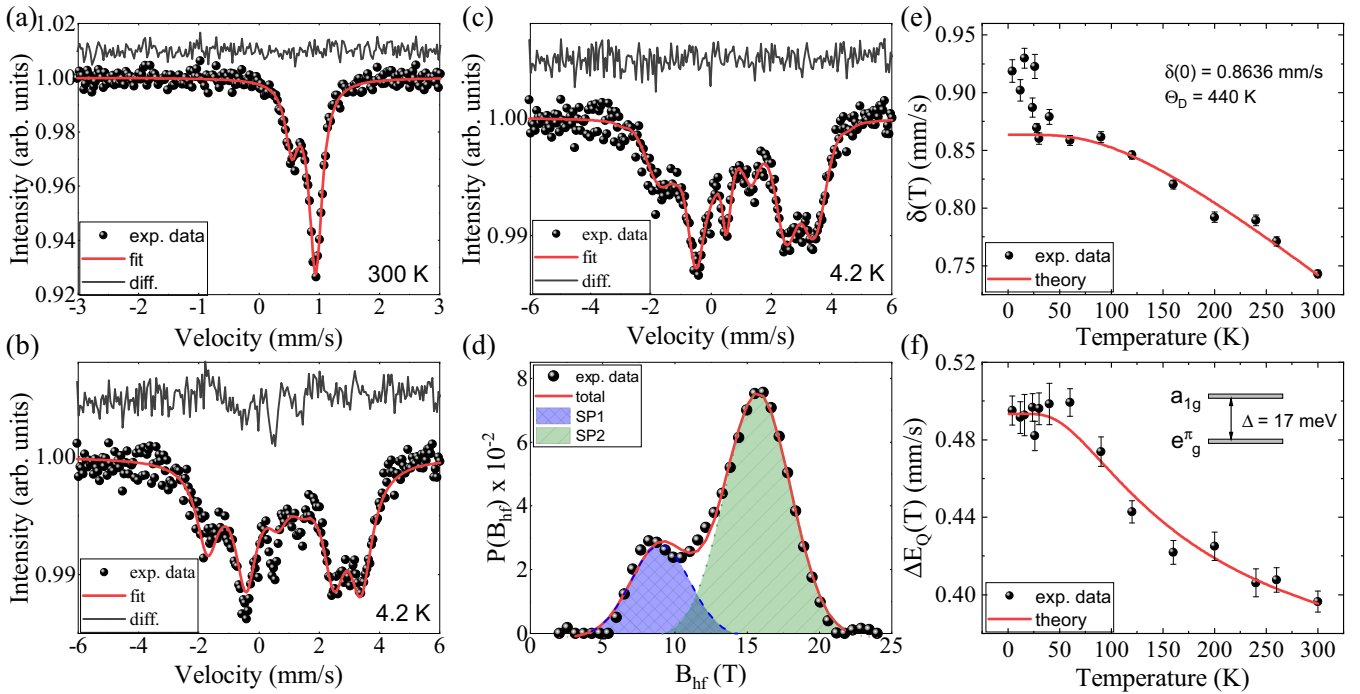


FIG. 3. (a) Room temperature Mössbauer spectrum together with theoretical fit assuming V_{zz} along c axis. (b) Mössbauer spectrum taken at 4.2 K. The data was fitted with only one subspectrum corresponding to the collinear single-Q state shown in Fig. 1(d). (c) Modeling the 4.2 K spectrum with a hyperfine field distribution by assuming a simple linear correlation between θ and B_{hf} (due to the out-of-plane anisotropy of B_{hf}), where θ is the angle between B_{hf} and V_{zz}/c axis. The determined probability profile showing two B_{hf} centers is shown in (d). The fitted Mössbauer hyperfine parameters, isomer shift $\delta(T)$, and quadrupole splitting $\Delta E_Q(T) = eQV_{zz}/2$, of $(\text{Co}_{0.99}^{57}\text{Fe})_{1/3}\text{NbS}_2$ crystals are shown as a function of temperature in (e) and (f), respectively. Solid line in (e) is theoretical curve calculated by the Debye model using a Debye temperature of $\Theta_D = 440$ K and $\delta(0) = 0.864$ mm/s. Solid line in (f) is theoretical curve calculated using Eq. (1) with $\Delta = 17$ meV as described in the text.

distribution by assuming a simple linear correlation between θ and B_{hf} (due to the out-of-plane anisotropy of B_{hf}), where θ is the angle between B_{hf} and V_{zz}/c axis. As shown in Fig. 3(c), the agreement between theory and experiment improves considerably. Most importantly, the determined hyperfine field distribution profile as shown in Fig. 3(d) exhibits a two peak feature having centers at ~ 9 T and ~ 16 T with a probability ratio close to 1:3. The resulting average $\langle \theta \rangle$ amounts to 52.7° , which is very close to the theoretical average value of 53° for the two subgroups of spins in the triple-Q state. This coincides exactly with our DFT predictions for the tetrahedral triple-Q magnetic ground state where two different B_{hf} s should be observed. That is, the eight atoms within the $2 \times 2 \times 1$ supercell are divided into two subgroups with a ratio of 1:3 due to the different spin orientations, namely two atoms with their spins along the c axis exhibiting a smaller $B_{\text{hf}} \sim 10$ T and the remaining six atoms with their spins forming an angle of $\sim 71^\circ$ with the c axis exhibiting a larger $B_{\text{hf}} \sim 16$ T. Therefore, our local Mössbauer spectroscopy measurements clearly support the triple-Q magnetic ordering, proposed for $\text{Co}_{1/3}\text{TaS}_2$ [17], over the domain averaged single-Q magnetic ordering for the title compound $\text{Co}_{1/3}\text{NbS}_2$.

The sufficiency of the above described fitting model can be seen from the overall good agreement between theory and the experimental data as shown in Figs. S8 and S9 in the Supplemental Material. The deduced temperature dependence of isomer shift $\delta(T)$ and quadrupole splitting $\Delta E_Q(T)$ are shown

in Figs. 3(e) and 3(f), respectively. A sudden increase of $\delta(T)$ can be observed upon entering the AFM ground state below $T_N = 28$ K, indicating an increase of the $3d$ electron density at the nucleus (stronger shielding effect of the s electrons by the $3d$ electrons). The theoretical line shown in Fig. 3(e) was calculated using the Debye model with a Debye temperature of $\Theta_D = 440$ K and $\delta(0) = 0.864$ mm/s. The determined quadrupole splitting is in the range of $0.4 \sim 0.5$ mm/s, which leads to V_{zz} values in the range of $2.4 \sim 3.0 \times 10^{21}$ V/m 2 . The temperature dependence of the ΔE_Q can be attributed to the temperature dependent valence contribution to the EFG resulting from the unequal population of $3d$ orbitals [48,49]. According to the crystal structure, the local symmetry of the intercalated $\text{Co}/^{57}\text{Fe}$ atoms is D_{3d} , which means that the $3d$ orbitals will split into the so-called doubly degenerated e_g^σ (d_{xz} , d_{yz}) and e_g^π (d_{xy} , $d_{x^2-y^2}$), and nondegenerated a_{1g} (d_{z^2}) states [50]. In this case, the ΔE_Q can be divided into a temperature independent part, E_{Q0} , and a temperature dependent part, $E_Q(T)$, that can be expressed as [48,49]

$$E_Q(T) = \sum_i (E_Q)^i e^{-\Delta_i/k_B T} / \sum_i e^{-\Delta_i/k_B T}, \quad (1)$$

where Δ_i is the separation energy between the involved orbitals and the sum runs over these orbitals (here we will consider only the low-lying e_g^π and a_{1g} orbitals). The fitted theoretical curve is shown in Fig. 3(f) and the determined energy separation between e_g^π and a_{1g} orbitals is ~ 17.3 meV.

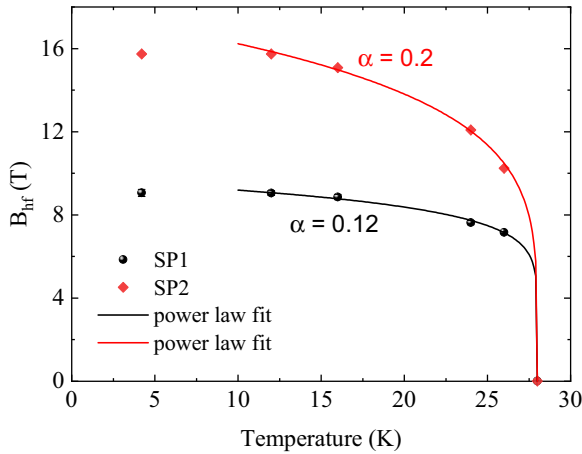


FIG. 4. Temperature dependence of the deduced hyperfine magnetic field of $(\text{Co}_{0.99}\text{Fe}_{0.01})_{1/3}\text{NbS}_2$ single crystals. Solid lines are fits with an empirical formula $B_{\text{hf}}(T) = B_0[1 - (T/T_N)]^\alpha$.

The temperature dependent $B_{\text{hf}}(T)$, determined by fitting the low temperature data with the hyperfine field distribution model described above are shown in Fig. 4. We used an empirical formula $B_{\text{hf}}(T) = B_0[1 - (T/T_N)]^\alpha$ to fit the data. The fitted results are $B_{\text{hf}}(0) = 9.7(3)\text{T}$ for the SP1 atoms and $B_{\text{hf}}(0) = 17.7(2)\text{T}$ for the SP2 atoms, and the determined transition temperature are both $\sim 28\text{K}$. The fitted critical exponents are ~ 0.12 and ~ 0.2 , respectively, which fall well into the universal window for two dimensional systems [51,52]. The observation of different values for the two species of atoms is interesting, the value of 0.12 for SP1 atoms is close to the theoretical value of 1/8 for the 2D Ising model while the value of 0.2 for SP2 atoms is close to the theoretical value 0.23 for the 2D XY model [51,52]. These results are again consistent with the local symmetries of the two species of atoms in the triple-Q state. However, due to the limited data points of our measurements, we can not determine the critical exponent more accurately and therefore it should be revisited in a future time with greater accuracy.

IV. DISCUSSION AND CONCLUSIONS

Understanding the observed AHE in $\text{Co}_{1/3}\text{NbS}_2$ requires (i) noncollinear, noncoplanar, or other possible magnetic textures [5,6]; or (ii) interplay between electronic and magnetic degrees of freedom, such as large Berry curvature embedded in the Dirac-like chiral fermions with weak symmetry breaking by SOC/ferromagnetic canting [18]. Tanaka *et al.* have argued that the weak ferromagnetism which appears along the

c axis is responsible for the emergence of the AHE by showing the simultaneously appearing/disappearing of the weak ferromagnetism and AHE [53]. Recently, Park *et al.* have shown that the similar compound $\text{Co}_{1/3}\text{TaS}_2$ actually orders in the so-called tetrahedral triple-Q magnetic state by ruling out the domain averaged single-Q state with nonzero AHE and weak ferromagnetic component along the c axis (M_z) [17]. Spin polarized neutron diffraction analysis by Takagi *et al.* also supports that both $\text{Co}_{1/3}\text{TaS}_2$ and $\text{Co}_{1/3}\text{NbS}_2$ order in the tetrahedral triple-Q magnetic state. Clearly, knowledge of the true magnetic ground state is the key to resolve all these possible scenarios to account for the observed AHE.

Our microscopic local probe measurements clearly support that the tetrahedral triple-Q state, proposed for $\text{Co}_{1/3}\text{TaS}_2$ and $\text{Co}_{1/3}\text{NbS}_2$ by neutron scattering [17,25], is the magnetic ground state. Then the resulting nonzero scalar spin chirality, $\langle \mathbf{S}_i \cdot \mathbf{S}_j \times \mathbf{S}_k \rangle$, explains naturally both the weak ferromagnetism along the c axis and the large AHE [22,23,54]. Due to the complexity of the magnetic structure of this system, we can not fully rule out other possibilities that may also produce the two different hyperfine magnetic fields with exact probability ratio of 1:3 in $\text{Co}_{1/3}\text{NbS}_2$. However, we do think that this is not likely since the tetrahedral triple-Q magnetic structure has been proposed by neutron diffraction for both $\text{Co}_{1/3}\text{NbS}_2$ [25] and $\text{Co}_{1/3}\text{TaS}_2$ [17], and the proposed magnetic ordering is the most symmetric one among other triple-Q states [17,24]. Moreover, the proposed triple-Q states have been shown by many theoretical works that they could be the state with lowest energy and can be used for the interpretation of the AHE observed in related materials [16,21–23,54–56]. Thus, as an important complement to the neutron scattering measurements, our results provide important insights not only to the magnetic structure but also the AHE in $\text{Co}_{1/3}\text{NbS}_2$ and other similar materials. Moreover, our work demonstrates a simple but effective procedure for identifying the exotic triple-Q state over the domain averaged single-Q state, not only applicable to the title compound but also for other materials such as the $\text{Na}_2\text{Co}_2\text{TeO}_6$ [26] compound, which is a subject of future works also for other local probing methods such as PAC and NMR [57], etc.

ACKNOWLEDGMENTS

Project supported by the National Natural Science Foundation of China (Grant No. 12247101) and the National Key Research and Development Program of China (Grants No. 2022YFB4101401 and No. 2022YFA1402704). The authors are grateful to the support provided by the Supercomputing Center of Lanzhou University.

- [1] Y. Togawa, T. Koyama, K. Takayanagi, S. Mori, Y. Kousaka, J. Akimitsu, S. Nishihara, K. Inoue, A. S. Ovchinnikov, and J. Kishine, Chiral magnetic soliton lattice on a chiral helimagnet, *Phys. Rev. Lett.* **108**, 107202 (2012).
 [2] D. Braam, C. Gomez, S. Tezok, E. V. L. de Mello, L. Li, D. Mandrus, H.-Y. Kee, and J. E. Sonier, Magnetic properties of the helimagnet $\text{Cr}_{1/3}\text{NbS}_2$ observed by μSR , *Phys. Rev. B* **91**, 144407 (2015).

- [3] Y. Togawa, Y. Kousaka, S. Nishihara, K. Inoue, J. Akimitsu, A. S. Ovchinnikov, and J. Kishine, Interlayer magnetoresistance due to chiral soliton lattice formation in hexagonal chiral magnet CrNb_3S_6 , *Phys. Rev. Lett.* **111**, 197204 (2013).
 [4] N. Kiyohara, T. Tomita, and S. Nakatsuji, Giant anomalous Hall effect in the chiral antiferromagnet Mn_3Ge , *Phys. Rev. Appl.* **5**, 064009 (2016).

- [5] N. J. Ghimire, A. S. Botana, J. S. Jiang, J. Zhang, Y.-S. Chen, and J. F. Mitchell, Large anomalous Hall effect in the chiral-lattice antiferromagnet CoNb_3S_6 , *Nat. Commun.* **9**, 3280 (2018).
- [6] G. Tenasini, E. Martino, N. Ubrig, N. J. Ghimire, H. Berger, O. Zaharko, F. Wu, J. F. Mitchell, I. Martin, L. Forró, and A. F. Morpurgo, Giant anomalous Hall effect in quasi-two-dimensional layered antiferromagnet $\text{Co}_{1/3}\text{NbS}_2$, *Phys. Rev. Res.* **2**, 023051 (2020).
- [7] Y. Tokura and N. Kanazawa, Magnetic skyrmion materials, *Chem. Rev.* **121**, 2857 (2021).
- [8] A. Fert, N. Reyren, and V. Cros, Magnetic skyrmions: Advances in physics and potential applications, *Nat. Rev. Mater.* **2**, 17031 (2017).
- [9] A. Fert, V. Cros, and J. Sampaio, Skyrmions on the track, *Nat. Nanotechnol.* **8**, 152 (2013).
- [10] R. Aoki, Y. Kousaka, and Y. Togawa, Anomalous nonreciprocal electrical transport on chiral magnetic order, *Phys. Rev. Lett.* **122**, 057206 (2019).
- [11] Y. Togawa, T. Koyama, Y. Nishimori, Y. Matsumoto, S. McVitie, D. McGrouther, R. L. Stamps, Y. Kousaka, J. Akimitsu, S. Nishihara, K. Inoue, I. G. Bostrem, V. E. Sinitsyn, A. S. Ovchinnikov, and J. Kishine, Magnetic soliton confinement and discretization effects arising from macroscopic coherence in a chiral spin soliton lattice, *Phys. Rev. B* **92**, 220412(R) (2015).
- [12] S. K. Karna, F. N. Womack, R. Chapai, D. P. Young, M. Marshall, W. Xie, D. Graf, Y. Wu, H. Cao, L. DeBeer-Schmitt, P. W. Adams, R. Jin, and J. F. DiTusa, Consequences of magnetic ordering in chiral $\text{Mn}_{1/3}\text{NbS}_2$, *Phys. Rev. B* **100**, 184413 (2019).
- [13] K. Lu, D. Sapkota, L. DeBeer-Schmitt, Y. Wu, H. B. Cao, N. Mannella, D. Mandrus, A. A. Aczel, and G. J. MacDougall, Canted antiferromagnetic order in the monoaxial chiral magnets $\text{V}_{1/3}\text{TaS}_2$ and $\text{V}_{1/3}\text{NbS}_2$, *Phys. Rev. Mater.* **4**, 054416 (2020).
- [14] S. Wu, Z. Xu, S. C. Haley, S. F. Weber, A. Acharya, E. Maniv, Y. Qiu, A. A. Aczel, N. S. Settin, J. B. Neaton, J. G. Analytis, and R. J. Birgeneau, Highly tunable magnetic phases in transition-metal dichalcogenide $\text{Fe}_{1/3+\delta}\text{NbS}_2$, *Phys. Rev. X* **12**, 021003 (2022).
- [15] Y. An, P. Park, C. Kim, K. Zhang, H. Kim, M. Avdeev, J. Kim, M.-J. Han, H.-J. Noh, S. Seong, J.-S. Kang, H.-D. Kim, and J.-G. Park, Bulk properties of the chiral metallic triangular antiferromagnets $\text{Ni}_{1/3}\text{NbS}_2$ and $\text{Ni}_{1/3}\text{TaS}_2$, *Phys. Rev. B* **108**, 054418 (2023).
- [16] H. Park, O. Heinonen, and I. Martin, First-principles study of magnetic states and the anomalous Hall conductivity of MNb_3S_6 ($M = \text{Co}, \text{Fe}, \text{Mn}, \text{and Ni}$), *Phys. Rev. Mater.* **6**, 024201 (2022).
- [17] P. Park, W. Cho, C. Kim, Y. An, Y.-G. Kang, M. Avdeev, R. Sibille, K. Iida, R. Kajimoto, K. H. Lee, W. Ju, E.-J. Cho, H.-J. Noh, M. J. Han, S.-S. Zhang, C. D. Batista, and J.-G. Park, Tetrahedral triple-Q magnetic ordering and large spontaneous Hall conductivity in the metallic triangular antiferromagnet $\text{Co}_{1/3}\text{TaS}_2$, *Nat. Commun.* **14**, 8346 (2023).
- [18] A. Zhang, K. Deng, J. Sheng, P. Liu, S. Kumar, K. Shimada, Z. Jiang, Z. Liu, D. Shen, J. Li, J. Ren, L. Wang, L. Zhou, Y. Ishikawa, Q. Zhang, G. McIntyre, D. Yu, E. Liu, L. Wu, C. Chen *et al.*, Chiral Dirac fermion in a collinear antiferromagnet, *Chin. Phys. Lett.* **40**, 126101 (2023).
- [19] S. S. P. Parkin, E. A. Marseglia, and P. J. Brown, Magnetic structure of $\text{Co}_{1/3}\text{NbS}_2$ and $\text{Co}_{1/3}\text{TaS}_2$, *J. Phys. C* **16**, 2765 (1983).
- [20] K. Momma and F. Izumi, *VESTA3* for three-dimensional visualization of crystal, volumetric and morphology data, *J. Appl. Crystallogr.* **44**, 1272 (2011).
- [21] C. D. Batista, S.-Z. Lin, S. Hayami, and Y. Kamiya, Frustration and chiral orderings in correlated electron systems, *Rep. Prog. Phys.* **79**, 084504 (2016).
- [22] I. Martin and C. D. Batista, Itinerant electron-driven chiral magnetic ordering and spontaneous quantum Hall effect in triangular lattice models, *Phys. Rev. Lett.* **101**, 156402 (2008).
- [23] Y. Kato, I. Martin, and C. D. Batista, Stability of the spontaneous quantum Hall state in the triangular Kondo-Lattice model, *Phys. Rev. Lett.* **105**, 266405 (2010).
- [24] J. Spethmann, S. Meyer, K. von Bergmann, R. Wiesendanger, S. Heinze, and A. Kubetzka, Discovery of magnetic single- and triple- \mathbf{q} states in $\text{Mn}/\text{Re}(0001)$, *Phys. Rev. Lett.* **124**, 227203 (2020).
- [25] H. Takagi, R. Takagi, S. Minami, T. Nomoto, K. Ohishi, M.-T. Suzuki, Y. Yanagi, M. Hirayama, N. D. Khanh, K. Karube, H. Saito, D. Hashizume, R. Kiyonagi, Y. Tokura, R. Arita, T. Nakajima, and S. Seki, Spontaneous topological Hall effect induced by non-coplanar antiferromagnetic order in intercalated van der Waals materials, *Nat. Phys.* **19**, 961 (2023).
- [26] W. G. F. Krüger, W. Chen, X. Jin, Y. Li, and L. Janssen, Triple- \mathbf{q} order in $\text{Na}_2\text{Co}_2\text{TeO}_6$ from proximity to hidden-SU(2)-symmetric point, *Phys. Rev. Lett.* **131**, 146702 (2023).
- [27] See Supplemental Material at <http://link.aps.org/supplemental/10.1103/PhysRevB.109.094401> for DFT calculation, sample preparation, and characterization details.
- [28] G. Kresse and J. Furthmüller, Efficient iterative schemes for ab initio total-energy calculations using a plane-wave basis set, *Phys. Rev. B* **54**, 11169 (1996).
- [29] G. Kresse and J. Furthmüller, Efficiency of ab-initio total energy calculations for metals and semiconductors using a plane-wave basis set, *Comput. Mater. Sci.* **6**, 15 (1996).
- [30] The Elk Code, <http://elk.sourceforge.net/>.
- [31] S. Sinnecker, L. D. Slep, E. Bill, and F. Neese, Performance of nonrelativistic and quasi-relativistic hybrid DFT for the prediction of electric and magnetic hyperfine parameters in ^{57}Fe Mössbauer spectra, *Inorg. Chem.* **44**, 2245 (2005).
- [32] H. Algaidi, C. Zhang, C. Liu, D. Zheng, Y. Ma, Y. Yuan, and X. Zhang, Thickness-tunable magnetic and electronic transport properties of the quasi-two-dimensional van der Waals ferromagnet $\text{Co}_{0.27}\text{TaS}_2$ with disordered intercalation, *Phys. Rev. B* **107**, 134406 (2023).
- [33] H. J. Monkhorst and J. D. Pack, Special points for Brillouin-zone integrations, *Phys. Rev. B* **13**, 5188 (1976).
- [34] S. Blügel, H. Akai, R. Zeller, and P. H. Dederichs, Hyperfine fields of $3d$ and $4d$ impurities in nickel, *Phys. Rev. B* **35**, 3271 (1987).
- [35] P. E. Blöchl, Projector augmented-wave method, *Phys. Rev. B* **50**, 17953 (1994).
- [36] A. I. Liechtenstein, V. I. Anisimov, and J. Zaanen, Density-functional theory and strong interactions: Orbital ordering in Mott-Hubbard insulators, *Phys. Rev. B* **52**, R5467 (1995).
- [37] S. L. Dudarev, G. A. Botton, S. Y. Savrasov, C. J. Humphreys, and A. P. Sutton, Electron-energy-loss spectra and the structural

- stability of nickel oxide: An LSDA+U study, *Phys. Rev. B* **57**, 1505 (1998).
- [38] J. P. Perdew, K. Burke, and M. Ernzerhof, Generalized gradient approximation made simple, *Phys. Rev. Lett.* **77**, 3865 (1996).
- [39] P. Liu, A. Zhang, J. Han, and Q. Liu, Chiral Dirac-like fermion in spin-orbit-free antiferromagnetic semimetals, *The Innovation* **3**, 100343 (2022).
- [40] M. Bottoni and H. Ebert, Decomposition of the relativistic hyperfine interaction operator: Application to the ferromagnetic alloy systems fcc $\text{Fe}_x\text{Ni}_{1-x}$, fcc $\text{Fe}_x\text{Pd}_{1-x}$, and fcc $\text{Co}_x\text{Pt}_{1-x}$, *Phys. Rev. B* **64**, 094417 (2001).
- [41] U. Gonser, *Microscopic Methods in Metals* (Springer, Berlin, Heidelberg, 1986).
- [42] P. Gülich, E. Bill, and A. X. Trautwein, *Mössbauer Spectroscopy and Transition Metal Chemistry* (Springer, Berlin, Heidelberg, 2011).
- [43] A. Sobolev, V. Rusakov, A. Moskvina, A. Gapochka, A. Belik, I. Glazkova, A. Akulenko, G. Demazeau, and I. Presniakov, ^{57}Fe Mössbauer study of unusual magnetic structure of multiferroic $3R\text{-AgFeO}_2$, *J. Phys.: Condens. Matter* **29**, 275803 (2017).
- [44] H. Wang, M. Wu, H. Zhou, B. Zhang, S. Hu, T. Ma, Z. Li, L. Qiao, T. Wang, and F. Li, Effect of hydrogen plasma implantation on the micro-structure and magnetic properties of $hcp\text{-Co}_{80}\text{Fe}_{16}\text{Ir}_4$ thin films, *Chin. Phys. B* **30**, 057505 (2021).
- [45] I. S. Lyubutin, M. A. Chuev, S. S. Starchikov, K. O. Funtov, and M. V. Lyubutina, Spiral magnetic structures with various helix parameters in langasite family compounds tested by Mössbauer spectroscopy, *J. Magn. Magn. Mater.* **504**, 166665 (2020).
- [46] S. Mangelsen, P. Zimmer, C. Näther, S. Mankovsky, S. Polesya, H. Ebert, and W. Bensch, Interplay of sample composition and anomalous Hall effect in Co_xNbS_2 , *Phys. Rev. B* **103**, 184408 (2021).
- [47] S. Mangelsen, J. Hansen, P. Adler, W. Schnelle, W. Bensch, S. Mankovsky, S. Polesya, and H. Ebert, Large anomalous Hall effect and slow relaxation of the magnetization in $\text{Fe}_{1/3}\text{TaS}_2$, *J. Phys. Chem. C* **124**, 24984 (2020).
- [48] R. Ingalls, Electric-field gradient tensor in ferrous compounds, *Phys. Rev.* **133**, A787 (1964).
- [49] Y. Li, J. Xue, S. Hu, and H. Pang, Mössbauer spectroscopy study of nematicity in $\text{Ba}(\text{Fe}_{0.962}\text{Cu}_{0.038})_2\text{As}_2$ single crystal: Enhanced orbital effect, *J. Phys.: Condens. Matter* **33**, 205602 (2021).
- [50] A. Rahman, M. Ur Rehman, M. Kiani, H. Zhao, J. Wang, Y. Lu, K. Ruan, R. Dai, Z. Wang, L. Zhang, J. Wang, and Z. Zhang, Critical behavior and phase diagram of layered ferromagnetic FeTa_3S_6 single crystals, *Phys. Rev. B* **105**, 144413 (2022).
- [51] A. Taroni, S. T. Bramwell, and P. C. W. Holdsworth, Universal window for two-dimensional critical exponents, *J. Phys.: Condens. Matter* **20**, 275233 (2008).
- [52] U. Köbler and A. Hoser, Critical magnetic behaviour in one and two dimensions, *J. Magn. Magn. Mater.* **311**, 523 (2007).
- [53] H. Tanaka, S. Okazaki, K. Kuroda, R. Noguchi, Y. Arai, S. Minami, S. Ideta, K. Tanaka, D. Lu, M. Hashimoto, V. Kandyba, M. Cattelan, A. Barinov, T. Muro, T. Sasagawa, and T. Kondo, Large anomalous Hall effect induced by weak ferromagnetism in the noncentrosymmetric antiferromagnet CoNb_3S_6 , *Phys. Rev. B* **105**, L121102 (2022).
- [54] S. Grytsiuk, J.-P. Hanke, M. Hoffmann, J. Bouaziz, O. Gomonay, G. Bihlmayer, S. Lounis, Y. Mokrousov, and S. Blügel, Topological chiral magnetic interactions driven by emergent orbital magnetism, *Nat. Commun.* **11**, 511 (2020).
- [55] O. Heinonen, R. A. Heinonen, and H. Park, Magnetic ground states of a model for $M\text{Nb}_3\text{S}_6$ ($M = \text{Co}, \text{Fe}, \text{Ni}$), *Phys. Rev. Mater.* **6**, 024405 (2022).
- [56] Ph. Kurz, G. Bihlmayer, K. Hirai, and S. Blügel, Three-dimensional spin structure on a two-dimensional lattice: $\text{Mn}/\text{Cu}(111)$, *Phys. Rev. Lett.* **86**, 1106 (2001).
- [57] Y. Tokunaga, Y. Homma, S. Kambe, D. Aoki, H. Sakai, E. Yamamoto, A. Nakamura, Y. Shiokawa, R. E. Walstedt, and H. Yasuoka, NMR evidence for triple- \vec{q} multipole structure in NpO_2 , *Phys. Rev. Lett.* **94**, 137209 (2005).